



Triple-cation perovskite solar cells for visible light communications

NATALIE A. MICA,¹ RUI BIAN,² PAVLOS MANOUSIADIS,¹ LETHY K. JAGADAMMA,¹ IMAN TAVAKKOLNIA,² HARALD HAAS,^{2,3}  GRAHAM A. TURNBULL,^{1,4}  AND IFOR D. W. SAMUEL^{1,5} 

¹Organic Semiconductor Centre, SUPA, School of Physics and Astronomy, St Andrews, Fife KY16 9SS, UK

²LiFi Research and Development Centre, Institute for Digital Communications, School of Engineering, University of Edinburgh, Edinburgh EH9 3FD, UK

³e-mail: H.Haas@ed.ac.uk

⁴e-mail: gat@st-andrews.ac.uk

⁵e-mail: idws@st-andrews.ac.uk

Received 3 April 2020; revised 22 May 2020; accepted 25 May 2020; posted 26 May 2020 (Doc. ID 393647); published 14 July 2020

Hybrid perovskite materials are widely researched due to their high absorptivity, inexpensive synthesis, and promise in photovoltaic devices. These materials are also of interest as highly sensitive photodetectors. In this study, their potential for use in visible light communication is explored in a configuration that allows for simultaneous energy and data harvesting. Using a triple-cation material and appropriate device design, a new record data rate for perovskite photodetectors of 56 Mbps and power conversion efficiencies above 20% under white LED illumination are achieved. With this device design, the -3 dB bandwidth is increased by minimizing the dominating time constant of the system. This correlation between the bandwidth and time constant is proved using measurements of time-resolved photoluminescence, transient photovoltage, and device resistance.

Published by Chinese Laser Press under the terms of the [Creative Commons Attribution 4.0 License](https://creativecommons.org/licenses/by/4.0/). Further distribution of this work must maintain attribution to the author(s) and the published article's title, journal citation, and DOI.

<https://doi.org/10.1364/PRJ.393647>

1. INTRODUCTION

Over recent years, hybrid perovskite solar cells have become an increasingly competitive technology for energy harvesting due to their high solar power conversion efficiencies reaching up to 25% [1], stability reaching several thousands of hours [2], and better performance than inorganic solar cells in low-intensity indoor lighting conditions [3–5]. In addition, perovskite solar cells can often be made by solution processing, giving the potential for manufacture by roll-to-roll coating. Hybrid perovskites respond strongly to light, making these materials useful in photodetectors in a wide range of applications [6,7].

Here, we explore the potential of hybrid organic–inorganic perovskites for visible light communication (VLC). VLC is a fast and secure method for wireless communication while avoiding increasing congestion in the radio-frequency spectrum. For this technology, ordinary light emitting diode (LED) lighting can be retrofitted with circuitry to act as a fast data transmitter, while photodetectors, typically in the form of avalanche or p-i-n photodiodes, collect the light to allow for data decoding. Solar cells can also be used as a VLC receiver with appropriate circuitry that detects the alternating current (AC) data input separately from the direct current (DC) lighting background. This allows for simultaneous data communication and energy harvesting and it has been explored with inorganic and organic

photovoltaics [8–11]. Within this application, perovskite solar cells could be flexible and offer much simpler fabrication than GaAs, with the potential for higher power conversion efficiency than organic solar cells [8,10].

While much of the attention for receivers has been on silicon photodetectors, perovskite devices have also recently been studied by various groups [12–17]. In these studies, the measured -3 dB bandwidths have ranged from 0.1 to 3.0 MHz depending on device area [6,12], structure [14,15], external bias [13,16,17], and active layer composition [12,17], while the highest data rate achieved was 1.0 Mbps [12]. Another study utilized an inorganic perovskite as a color-converter for a perovskite-silicon photoreceiver, which achieved impressive data transmission rates of 34 Mbps [18]. From these studies, the magnitude of the bandwidth for perovskite photodetectors has been attributed to several different mechanisms. While these results could be adequate for transmitting text or audio-based data, these photodetectors do not use their fundamental benefit of harvesting data and energy at the same time.

In this paper, we demonstrate data transfer of 56 Mbps to perovskite solar cells used in a configuration that allows for communication and power generation concurrently. The cells are fabricated using triple-cation perovskites and optimized for VLC application by varying the active layer thickness over a

large range. These devices are then put into a circuit to allow for the measurement of their bandwidth, data rate, and bit error ratio (BER). This circuitry allows for the devices to be held under zero bias, with a small load resistor to allow for the exploitation of their ability to collect data and energy simultaneously [19]. By varying the perovskite thickness over such a large range, we are able to identify that the RC time constant is controlling the bandwidth, which is proved using transient photovoltage and internal resistance measurements. Within this paper, we also study the performance of these devices under white LED illumination that could be used within a real indoor VLC setup as well as a red laser used for testing their communication capability.

2. RESULTS

A. Solar Cell Performance

In this study, the triple-cation perovskite $\text{Cs}_{0.06}\text{MA}_{0.15}\text{FA}_{0.79}\text{Pb}(\text{I}_{0.85}\text{Br}_{0.15})_3$ was used due to its high power conversion

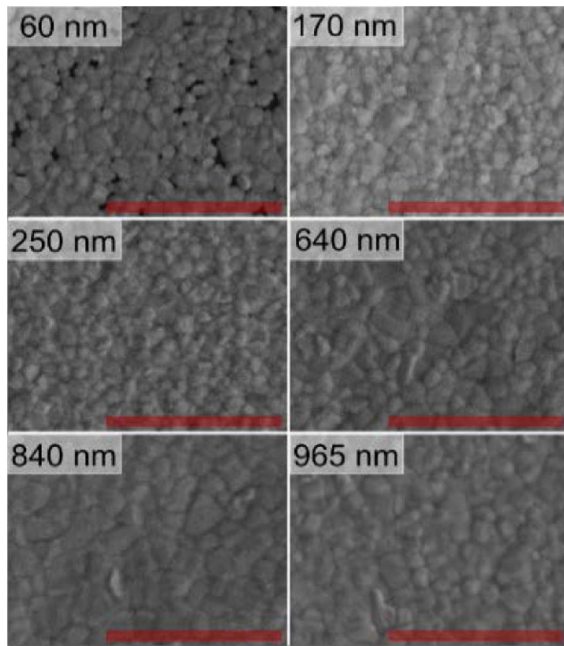


Fig. 1. SEM images of triple-cation perovskite films for all thicknesses. The red bar corresponds to a length of 2 μm .

efficiency reported elsewhere and higher bandwidth compared with MAPbI_3 or $\text{MA}_{0.15}\text{FA}_{0.85}\text{Pb}(\text{I}_{0.85}\text{Br}_{0.15})_3$ [17,20]. To identify the factors controlling the device time constant and to maximize the device bandwidth and data rate, a wide range of active layer thicknesses were fabricated and tested. These range from 60 to 965 nm and were made using a single spin-coating method, with antisolvent washing, by varying spin speeds and solution concentration. Figure 1 presents scanning electron microscopy (SEM) images of the perovskite films, which show that the microscopic film quality did not change substantially with these different spin-coating processes. Here, we utilized an n-i-p stacked structure for the devices of the form: $\text{ITO}/\text{SnO}_2/\text{perovskite}/\text{Spiro-OMeTAD}/\text{Au}$.

The indoor energy harvesting performance of these devices measured under illumination from a typical white LED with 0.9 mW/cm^2 incident power is reported in Table 1 and Fig. 2. The highest power conversion efficiency current density-voltage (J-V) curves are shown in Fig. 2(a). The performance of the same cells under AM 1.5 solar illumination is given in Appendix A Table 7. Under low-intensity LED lighting, the solar cells exhibit power conversion efficiencies (PCEs) in the range of 18%–21% for 170–640 nm thick devices. This enhanced performance compared with other thicknesses is due to their high FF and V_{oc} . As the active layer thickness is increased, the V_{oc} showed a significant drop. We attribute this to an increase in charge recombination due to roughening at the perovskite–Spiro-OMeTAD interface for thicker perovskite films. Evidence of this roughening for the 840 and 965 nm thick perovskite films is shown in Fig. 3, where large-scale ridges form on the surface due to the low spin-coating speeds used for their fabrication.

The external quantum efficiency (EQE) spectra for all perovskite devices with different thicknesses are shown in Fig. 2(b). The EQE spectrum changes shape as the perovskite film thickness increases, flattening out at thicknesses of 640 nm and above. The most dramatic changes in the spectrum are seen for the 60 to 250 nm devices, where the EQE has two peaks around wavelengths 400 and 600–650 nm. Similar changes in the EQE spectrum have been reported previously in organic solar cells for varying thickness and are attributed to parasitic absorption of the other layers in the device and the nonuniform optical excitation field within the active layer [21].

To assess the capability of these devices for simultaneous energy and data harvesting, the solar cell performance was tested under the lighting conditions subsequently used for

Table 1. Cell Performance of Triple-Cation Devices with Varied Active Layer Thickness Using a White LED with an Incident Optical Power of 0.9 mW/cm^2 ^{a,b}

Perov. Thickness [nm]	Best PCE [%]	PCE [%]	FF [%]	J_{SC} [mA/cm^2]	V_{OC} [V]	R_{S} [$\text{k}\Omega \cdot \text{cm}^2$]	R_{SH} [$\text{k}\Omega \cdot \text{cm}^2$]
60	2.9	2.4 ± 0.6	41 ± 2	0.07 ± 0.01	0.71 ± 0.11	4.3 ± 0.8	26.9 ± 7
170	18.7	16.3 ± 1.8	71 ± 5	0.22 ± 0.01	0.92 ± 0.02	0.6 ± 0.2	143 ± 80
250	20.3	18.2 ± 2.7	72 ± 9	0.25 ± 0.01	0.92 ± 0.02	0.7 ± 0.1	99.1 ± 40
640	21.4	19.7 ± 1.1	72 ± 2	0.27 ± 0.01	0.92 ± 0.01	0.5 ± 0.1	81.3 ± 20
840	14.9	13.6 ± 1.2	57 ± 3	0.25 ± 0.01	0.87 ± 0.01	0.8 ± 0.5	21.6 ± 5
965	13.8	12.6 ± 1.2	57 ± 2	0.23 ± 0.02	0.86 ± 0.02	0.9 ± 0.2	10.7 ± 4

^aHere, the device power conversion efficiency (PCE), fill factor (FF), short circuit current (J_{SC}), open circuit voltage (V_{OC}), series resistance (R_{S}), and shunt resistance (R_{SH}) are shown.

^bThe error within this table is the standard deviation of four to seven devices averaged together.

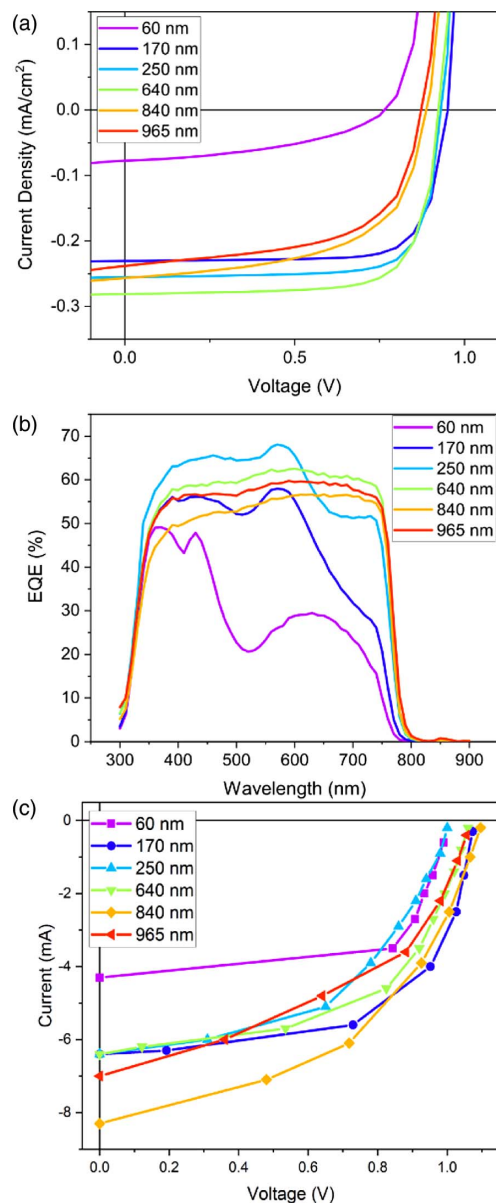


Fig. 2. Triple-cation perovskite devices with their (a) best J-V curves under 0.9 mW/cm^2 indoor white LED illumination, (b) EQE, and (c) I-V curves under 50 mW red laser (660 nm) illumination.

VLC experiments. A red (660 nm) laser diode with an output power of 50 mW was incident on the solar cell with a variable resistor across the solar cell to measure the I-V curve. As seen in Table 2, the PCE is in the range of 6%–9% under the full (50 mW) power used in the VLC setup. I-V curves produced with this laser illumination are shown in Fig. 2(c). In Table 2, we also estimate the EQE under this high-intensity illumination condition and note that these values are lower than those measured under lower intensity conditions, as reported in Fig. 2(b). The lower EQE and PCE values under the laser illumination could be due to higher recombination losses and increased resistive losses at higher light intensity, as shown in perovskite devices elsewhere [22–24]. Nevertheless, under this illumination, the devices could generate 3–5 mW of power,

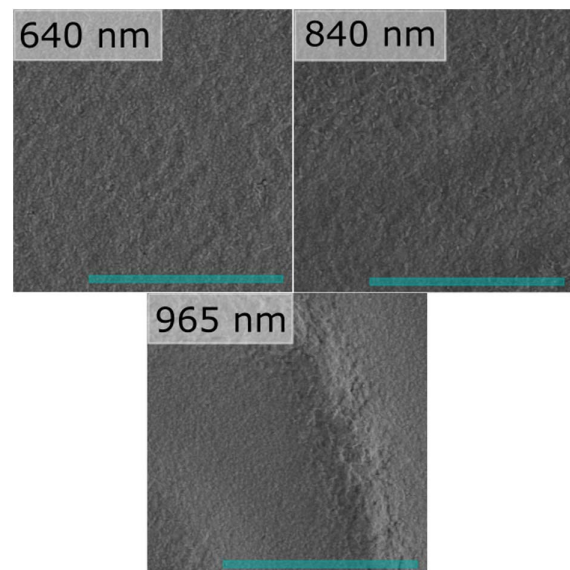


Fig. 3. Low-magnification SEM images of the three thickest triple-cation perovskite films. The blue scale bar represents a length of $10 \mu\text{m}$.

Table 2. External Quantum Efficiency of Triple-Cation Solar Cells under 660 nm Low Intensity and Laser Illumination, and Power Conversion Efficiency and Power Generated under 50 mW Laser Power

Perov. Thickness [nm]	EQE under Low Intensity [%]	EQE with Red Laser [%]	PCE with Red Laser [%]	Power Generated [mW]
60	28	16	6.1	3.1
170	39	24	9.0	4.5
250	53	24	6.5	3.3
640	61	24	7.7	3.9
840	56	31	8.8	4.4
965	59	26	6.7	3.3

which is enough to power a typical wireless sensor used for the Internet of Things [25,26].

B. VLC Results

To characterize the capability of these triple-cation devices for VLC, all solar cells were mounted 40 cm from a red (660 nm) laser diode with an incident power of 50 mW . This laser was focused onto the active area of the cell using two lenses at the transmitter and receiver sides. A sequence of random data was transmitted by the laser using the DC-biased optical orthogonal frequency division multiplexing (DCO-OFDM) digital modulation technique. The signal is detected by a single perovskite cell, and the output current of the cell is split into its DC and AC components, respectively, for energy harvesting and data detection. The AC component is captured by an oscilloscope and sent to a computer for analysis. A training sequence is used for estimating the system frequency response and signal-to-noise ratio (SNR) at various frequency bands. The bandwidth

of the system is determined by the perovskite solar cells, as other components (laser, oscilloscope, etc.) are significantly faster (i.e., -3 dB bandwidth higher than several hundreds of MHz). Based on the system frequency response and SNR, random data are transmitted, and the data rates achieved and associated bit error ratios (BERs) are measured [27,28]. As DCO-OFDM with adaptive bit loading is used, the achievable data rate will depend on the SNR at each subcarrier across the whole used frequency range but not on the -3 dB bandwidth of the device. Examples for the measured frequency response and bit loading for each perovskite thickness device are shown in Appendix B, Figs. 6 and 7.

The resulting -3 dB bandwidth and data rate are presented in Fig. 4 for devices of each perovskite thickness. Table 3 lists the average bandwidth, data rate, and BER. All BER values are below the hard decision forward-error correction coding threshold of 0.0047, which indicates that error-free detection is achievable by a 6.25% coding overhead [29]. Here, it is seen that the average bandwidth increases as the active layer thickness increases from 114 to 400 kHz, with a maximum measured bandwidth of 586 kHz for the 965 nm devices. This bandwidth magnitude is comparable with that reported

Table 3. Average and Standard Deviation of -3 dB Bandwidth, Data Rate, BER, and Number of Measured Samples of Triple-Cation Photodetectors with Varied Active Layer Thickness

Perov. Thickness [nm]	Bandwidth [kHz]	Data Rate [Mbps]	BER	Sample Size
60	114 ± 5	31 ± 4	2.8×10^{-3}	10
170	211 ± 71	32 ± 5	3.3×10^{-3}	8
250	259 ± 30	49 ± 4	3.0×10^{-3}	13
640	367 ± 100	43 ± 7	3.0×10^{-3}	12
840	386 ± 55	24 ± 1	3.2×10^{-3}	14
965	400 ± 73	33 ± 4	3.0×10^{-3}	21

elsewhere for triple-cation or similar perovskites, considering the cell active area of 6.5 mm^2 [6]. We note that the bandwidth achieved by Salamandra *et al.* was 800 kHz for a triple-cation perovskite device, which was slightly higher than that measured here [17]. However, the bandwidth from their study was determined by applying a small reverse bias on the solar cell, which increases the achievable bandwidth but does not allow for energy harvesting. In the current study, the highest data rate was achieved by the 250 nm thick perovskite layer devices. This data rate reached 56 Mbps and, to the best of the authors' knowledge, is the highest data rate for a perovskite receiver reported thus far.

3. DISCUSSION

A. Limitation of Bandwidth

Figure 4 highlights a clear trend in the bandwidth as the perovskite film thickness changes. It is known that perovskite films contain slow-moving mobile ions that are unable to react quickly to rapid changes in external bias [30]. This leads to the hysteresis in J-V curves that is commonly found in perovskite solar cells and it has been suggested that it could limit the photodetector bandwidth to the sub-MHz regime [6,17]. However, theoretical studies using a wide frequency range in impedance spectroscopy have seen these ions contribute in the low-frequency range of 10^{-3} – 10^2 Hz [31]. Above this frequency range, the ions are not able to adequately respond and cause a change in the output current of the solar cell, due to their large size. Because of this, mobile ions are not believed to limit the response of the photodetectors in high-frequency ranges above 1 kHz and certainly not at even higher frequency where the -3 dB bandwidth occurs.

Another explanation could be due to the intrinsic properties of the materials used in these devices: the low mobility of the organic hole transporting layer of Spiro-OMeTAD [32]. While organic semiconductors have charge mobilities orders of magnitude lower than perovskites, OLEDs and organic solar cells utilized in previous VLC studies have achieved bandwidths in the MHz region [8]. Because of this, it seems unlikely that the presence of an organic semiconductor limits the bandwidths reported here. As well, if the transit time of charge carriers within the Spiro-OMeTAD did limit the device bandwidth, then we would not expect to change the frequency response by changing the perovskite layer thickness. This is not what

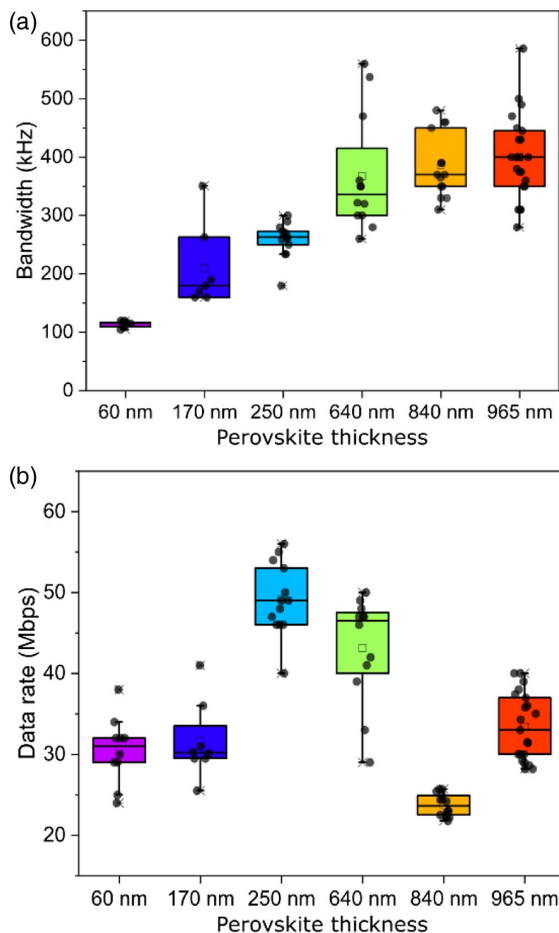


Fig. 4. (a) Box and whisker distributions of the -3 dB bandwidth and (b) achieved data rate for perovskite devices with varied active layer thickness. Here, the mean of the data is represented as a square, the median a solid line, and the ends of the box represent the 25%–75% range.

we observe in Fig. 4, which shows a dependence on achievable bandwidth with perovskite thickness.

In general, the lifetime of charge carriers within solar cells is sought to be maximized to allow for better collection efficiency and reduced charge recombination [33,34]. However, the charge lifetime being very long is thought to perhaps limit how quickly the device can respond to rapid changes in light level, thus limiting the photodetector bandwidth. To determine if this lifetime could be a limiting factor for these solar cells, time-resolved photoluminescence (TRPL) measurements were performed on devices to estimate the charge carrier lifetime. The extracted lifetimes (using a double-exponential decay fit) are listed in Table 4, and we compare the longer lifetime components for our discussion. The lifetimes fitted from these curves ranged from 8 ns for the 60 nm thick film to 126 ns for a thickness of 965 nm. If this lifetime is used to estimate the upper limit of the bandwidth, the 60 nm devices would have a bandwidth of 19.3 MHz, and the 965 nm thick devices have a bandwidth of 1.3 MHz. Both limits and their trend with perovskite thickness do not follow with what is observed here. Therefore, there must be a different physical mechanism that limits these devices.

Instead, these devices could be described as a first-order low-pass filter and limited by their RC time constant. As the active layer thickness increases, the geometric capacitance of the device is expected to decrease, leading to a lower time constant and a faster bandwidth. To test this, the RC time constant of these perovskite solar cells is explored in detail in the following section using multiple methods for measuring and estimating the capacitance.

Table 4. Coefficients (B_1, B_2) and Lifetimes (τ_1, τ_2) Extracted from the Two-Exponential Fit of TRPL Data for All Perovskite Devices of Varied Active Layer Thickness^a

Perov.				
Thickness [nm]	$B_1 [10^3]$	τ_1 [ns]	$B_2 [10^3]$	τ_2 [ns]
60	91.3	2.0	4.6	8.2
170	101.3	4.2	10.7	11.5
250	9.0	8.1	0.2	28.1
640	7.1	18.2	1.5	83.4
840	5.5	23.6	3.8	70.7
965	5.3	59.4	3.9	125.5

^aEquation used for this fitting was of the form: $I_{PL}(t) = B_1 e^{-t/\tau_1} + B_2 e^{-t/\tau_2}$.

B. RC Time Constant Estimation

An initial estimation of the solar cell's RC time constant can be made by using its bandwidth and measuring the resistance. For an RC low-pass filter, the -3 dB bandwidth, $f_{-3\text{ dB}}$, is given by $f_{-3\text{ dB}} = 1/(2\pi RC)$, such that R is the device resistance and C is its capacitance. The cell capacitance can be subsequently calculated with the knowledge of the resistance. This resistance is calculated by measuring the cell voltage under open-circuit conditions, then putting a load resistor in series, and measuring the voltage again. Calculating this can be done using the following approximation:

$$R = R_0(V_{oc}/V_{load} - 1).$$

Here, R is the device resistance, R_0 is the load resistance, and V_{load} is the output voltage of the solar cell when the load resistor is connected. Table 5 presents values for $f_{-3\text{ dB}}$, R , and C under the “bandwidth estimation” columns. It is seen that the RC time constant is a maximum for the thinnest devices and decreases steadily as the perovskite thickness increases.

To assess if the RC time constant is what limits the bandwidth, transient photovoltage tests were performed. In this measurement, the solar cell is illuminated by a square-wave light signal of frequency 200 kHz, and its output voltage as a function of time is measured. Fitting the rise of this curve with an exponential allows for the extraction of an RC time constant. Example data from this measurement and the extracted time constants as a function of perovskite thickness are shown in Fig. 5. Results from this fitting are given in Table 5 under the “transient photovoltage” columns. The results show that the RC time constants agree well with the values extracted from the bandwidth estimation.

Using the time constant from transient photovoltage measurements, the corresponding bandwidth can be calculated and is shown in the final column of Table 5. These values show bandwidths only marginally higher than those in Fig. 4, leading to the conclusion that the VLC performance of these solar cells is limited by their RC time constant, rather than by other mechanisms. For practical application, this implies that perovskite solar cells for VLC need to have their active layers carefully tuned to allow for higher achievable bandwidth while still taking care to avoid gaining too much resistance to maximize the data rate. Devices can also have their time constant optimized

Table 5. Measured Device Resistance, Calculated Capacitance, and RC Time Constant for Triple-Cation Devices of Varied Active Layer Thickness Using Two Methods: Bandwidth Estimation and Transient Photovoltage

Perov. Thickness [nm]	Bandwidth Estimation			Transient Photovoltage	
	$RC = 1/(2\pi f_{-3\text{ dB}})$ [ns]	Cell Resistance [Ω]	Capacitance [nF]	Fitted RC Time Const. [ns]	Calculated $f_{-3\text{ dB}}$ [kHz]
60	1485	271	5.5	1140	142
170	569	138	4.1	570	285
250	385	135	2.9	390	415
640	293	187	1.6	280	582
840	264	239	1.1	260	606
965	221	269	0.8	230	700

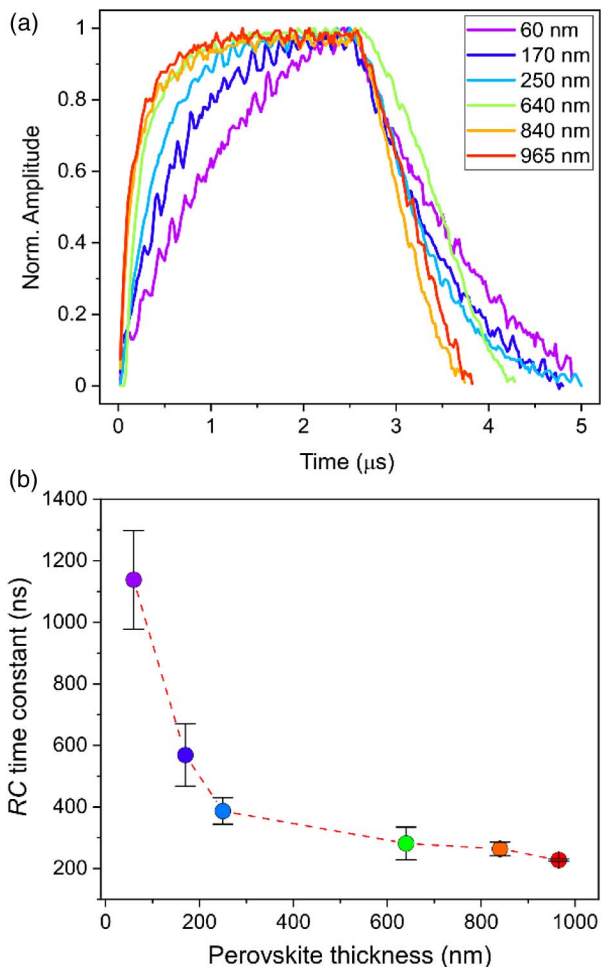


Fig. 5. (a) Transient photovoltage measurements for triple-cation perovskite solar cells with varied thickness. (b) Fitted RC time constant from this measurement.

by adjusting the active area; reducing this too much, however, could result in larger noise and poor data rate.

4. CONCLUSIONS

In this study, triple-cation perovskite solar cells are optimized for VLC applications by varying the active layer thickness over an order of magnitude. This study is the first of its kind to show these devices in a configuration that allows for simultaneous energy and data harvesting. Here, it is observed that the device bandwidth increases with perovskite thickness, and the highest data rate is achieved for the 250 nm thick perovskite solar cells using an OFDM signal. To the best of the authors' knowledge, this average data rate of 49 Mbps and maximum of 56 Mbps are the highest reported for perovskite photodetectors thus far. Using several measurements, it is shown here that these solar cells have bandwidth limited by their RC time constant. Our results suggest that hybrid perovskite solar cell technology is promising for VLC due to its high-power conversion efficiency and competitive data transmission rates.

5. EXPERIMENTAL METHODS

A. Solar Cell Fabrication

Perovskite precursor solutions were prepared in a N_2 glovebox approximately 4 h before use. Triple-cation stoichiometry was achieved by combining CsI (0.07 mol) + FAI (1.1 mol) + MABr (0.2 mol) + PbBr_2 (0.2 mol) + PbI_2 (1.2 mol) with DMF (800 μL) and DMSO (200 μL). Finished solar cells had an n-i-p structure: ITO/ SnO_2 / $\text{Cs}_{0.06}\text{MA}_{0.15}\text{FA}_{0.79}\text{Pb}(\text{I}_{0.85}\text{Br}_{0.15})_3$ /Spiro-OMeTAD/Au (60–80 nm). ITO glass substrates (Xin Yan Tech. Ltd.) were cleaned in an ultrasonic bath with a detergent solution (Hellmanex III), acetone, and then isopropyl alcohol for 10 min each. These substrates were then dried with N_2 and then plasma ashed (GaLa Instrumente GmbH) with O_2 gas for 3 min. A SnO_2 solution was prepared by diluting a stock nanoparticle solution (Alfa Aesar) in a 1:6.5 volume ratio with DI water, vortex mixed to ensure mixing. This solution was then spun onto the cleaned substrates at 3000 r/min for 30 s, and the film was annealed at 150°C for 30 min. The SnO_2 -coated substrates were then transferred into a N_2 glovebox for perovskite spin coating. To form the large range of perovskite thicknesses, the precursor concentration and spin speed were adjusted. All conditions to form the films used in this study are included in Table 6.

All films underwent an antisolvent washing step using chlorobenzene 10 s before the end of the spinning time, and then were annealed at 100°C for 1 h. The Spiro-OMeTAD solution was prepared at a 100 mg/mL concentration in chlorobenzene and doped with tBP (36 μL , Sigma Aldrich) + Li-TFSI (20 μL , 517 mg/mL in acetonitrile) + FK209 (8 μL , 376 mg/mL in acetonitrile). All solutions for this film were prepared just before use with a vortex mixer, and the final solution was spun at 4000 r/min for 30 s. This film was then allowed to oxygen dope for more than 12 h before being put into an evaporator for gold electrode deposition. The evaporator was pumped down to a pressure of 1×10^{-6} – 5×10^{-6} mbar and 60 nm of gold was thermally evaporated at a rate of 0.05 nm/s. The ITO electrode in these devices was 115 nm thick, the SnO_2 layer was 30 nm thick, and the Spiro-OMeTAD film was approximately 250 nm thick.

B. Solar Cell Performance

Performance was measured using an AM 1.5 solar simulator and a Keithley 2400 source meter to supply the bias voltage and measure current. EQE was calibrated using a photodiode, and the measurement was made using a Bentham lamp (Model 605) to send light through a monochromator (Bentham TMc300) connected to a fiber-couple. This fiber was set at the calibrated height, and a Keithley 6517A captured the output current from the solar cell. Performance for indoor lighting was tested using a white LED (UltraFire, CREEXML-T6) controlled by a function generator (Keithley 3390) with variable output voltage to adjust the output light intensity. The irradiance level was measured using an RK5710 power radiometer and optometer P9710. The same Keithley 2400 source meter for solar simulator performance was used to measure device performance under white LED illumination.

Table 6. Spin Coating Conditions for the Triple-Cation Perovskite Film Formation^a

Perovskite Thickness [nm]	Precursor Solution Concentration [mol/L]	Spin-Coating Condition
60	0.25	6000 r/min (40 s)
170	0.25	1000 r/min (40 s)
250	0.5	2000 r/min (10 s) + 6000 r/min (30 s)
640	1	2000 r/min (10 s) + 6000 r/min (30 s)
840	1	1400 r/min (40 s)
965	1	1000 r/min (40 s)

^aAll films had an antisolvent washing step using chlorobenzene 10 s before the end of the spinning time.

To calculate the power conversion efficiency of the I-V curves produced under red laser illumination, the curves were fitted to a modified ideal diode equation:

$$I = I_0 \left(e^{\frac{qV}{nk_B T}} - 1 \right) - I_{ph},$$

where q is the charge of an electron, k_B is Boltzmann's constant, T is temperature, and n is a fitting parameter to correct for the nonideal nature of the devices. This equation for each perovskite solar cell was multiplied by V to find the maximum power point, which was then used to calculate the power conversion efficiency for the device.

C. Bandwidth and Data Rate Measurements

A DCO-OFDM scheme is used for measuring the system bandwidth and estimating the achievable data rate. Due to the low-pass frequency response of the system, adaptive bit and energy loading is used for estimating the maximum achievable data rate. Details of the communication technique can be found in Refs. [27,28] and references therein. A communication system is set up for the measurement in the lab. On the transmitter side, a red laser (Thorlabs, HL6544FM) with a central wavelength of 660 nm is used as the light source. The DC bias value supplied by a bench power supply (TENMA 72-10505) and the AC signal generated by an arbitrary waveform generator (AWG, Keysight 81180A) are combined in a bias-Tee (Mini-Circuit, ZFBT-4R2GW+) and sent to the laser. On the receiver end, a single perovskite cell is used for capturing the optical signal. The output is connected to a custom-designed receiver circuit, which contains two branches: one branch with an inductor for energy harvesting and another

branch with a capacitor for data detection. The received AC signal is captured by an oscilloscope (Keysight, MSO7104B) and sent to a computer, where the data are processed offline in MATLAB software.

D. TRPL Measurement

Time-resolved PL was captured using an Edinburgh Instruments fluorimeter with excitation using a 640 nm laser. For this measurement, devices with the complete interlayer structure were used to determine the charge lifetime within these solar cells. All fitting was done using the software for the Edinburgh Instrument control and measurement.

E. Transient Photovoltage

A similar setup to the one described for the bandwidth and data rate measurements was used. The output of each perovskite cell is directly captured by the oscilloscope without any additional circuit at the receiver. The estimation of RC constant is performed in MATLAB software. Square waves with different frequencies and peak-to-peak values have been used for the measurements, and all the results are consistent.

APPENDIX A

The main text presents solar cell results under conditions most relevant to VLC, i.e. illumination by an LED or communications laser. Here shows the solar cell performance of these devices under standard AM 1.5 solar simulator light. Table 7 shows the performance of these triple cation perovskite devices with the voltage scanned in forward (short to open circuit) and reverse (open to short circuit) sweeping directions.

Table 7. Solar Cell Performance of Triple-Cation Perovskite Devices in Forward and Reverse Scans, under AM 1.5 Solar Simulator Illumination

Thickness [nm]	Best PCE [%]	PCE [%]	FF [%]	J_{sc} [mA/cm ²]	V_{oc} [V]	R_S [$\Omega \cdot \text{cm}^2$]	R_{SH} [k $\Omega \cdot \text{cm}^2$]
60	6.17	5.3 ± 0.9	65.5 ± 9.5	7.6 ± 0.6	1.07 ± 0.02	21.4 ± 14.9	50.0 ± 115.0
60 (reverse)	6.00	5.1 ± 0.7	66.8 ± 3.8	7.5 ± 0.6	1.01 ± 0.04	14.7 ± 4.7	50.0 ± 125.0
170	10.27	9.3 ± 0.9	58.9 ± 5.0	14.7 ± 1.3	1.07 ± 0.02	11.8 ± 3.4	30.0 ± 50.0
170 (reverse)	10.82	8.0 ± 1.6	56.3 ± 6.5	14.2 ± 1.3	0.99 ± 0.05	12.1 ± 3.4	2.0 ± 1.8
250	13.24	12.0 ± 1.2	69.5 ± 7.3	16.6 ± 0.8	1.04 ± 0.02	6.8 ± 4.3	16.0 ± 30.0
250 (reverse)	12.09	9.2 ± 1.2	58.3 ± 5.1	16.3 ± 0.9	0.96 ± 0.03	10.0 ± 1.9	28.0 ± 70.0
640	12.79	11.3 ± 1.1	58.9 ± 4.2	19.2 ± 0.8	0.99 ± 0.02	8.5 ± 1.9	1.2 ± 0.7
640 (reverse)	11.22	10.0 ± 0.8	57.3 ± 3.4	19.0 ± 0.7	0.92 ± 0.02	11.6 ± 2.4	1.0 ± 0.8
840	12.22	10.7 ± 0.9	55.1 ± 3.2	19.2 ± 1.1	1.01 ± 0.03	9.3 ± 1.8	1.3 ± 0.8
840 (reverse)	10.79	9.2 ± 1.5	52.0 ± 6.1	19.1 ± 1.1	0.92 ± 0.04	12.5 ± 2.3	0.8 ± 0.4
965	10.69	9.9 ± 0.4	53.4 ± 2.1	19.1 ± 1.0	0.97 ± 0.01	10.4 ± 1.5	1.0 ± 0.8
965 (reverse)	10.56	9.8 ± 0.6	56.3 ± 3.3	19.1 ± 0.7	0.91 ± 0.01	12.5 ± 1.3	60.0 ± 160.0

APPENDIX B

DCO-OFDM is an adaptive bit-loading technique for transferring data to a receiver. Because of this, the signal to noise ratio (SNR) of the receiver over a wide frequency range will determine its achievable data rate, rather than just having a direct relation with the bandwidth. Figure 6 shows example SNR curves for each perovskite device of varied active layer thickness, and Fig. 7 shows example bit loading based on the SNR.

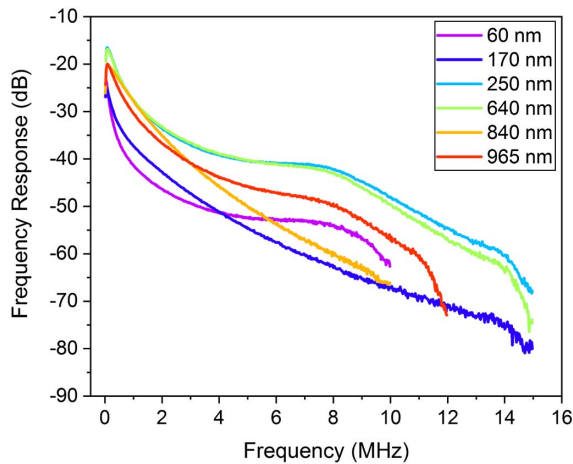


Fig. 6. Example frequency response for each perovskite thickness device.

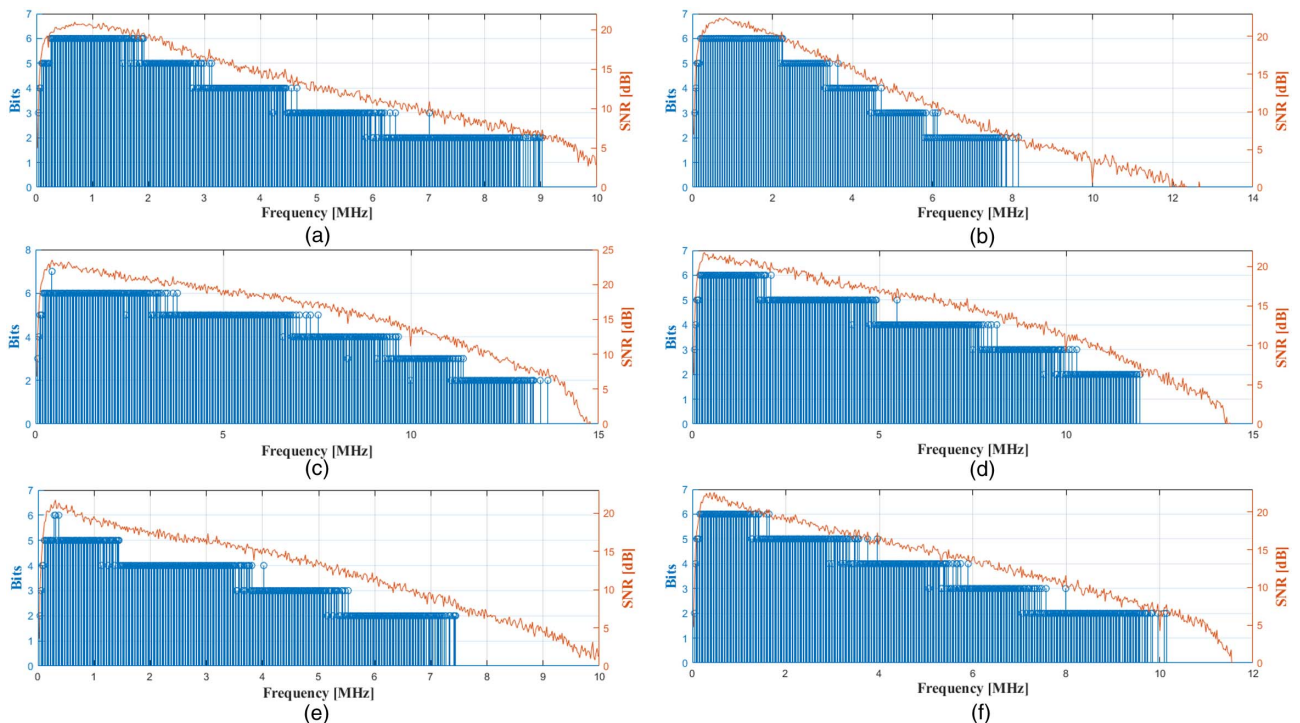


Fig. 7. Example of bit loading from one measurement of each thickness: (a) 60 nm, (b) 170 nm, (c) 250 nm, (d) 640 nm, (e) 840 nm, (f) 965 nm.

Funding. Engineering and Physical Sciences Research Council (EP/L015110/1, EP/L017008/1, EP/R007101/1); European Commission (MCIF 745776).

Acknowledgment. We are grateful to J. A. Smith and D. G. Lidzey for useful discussions on interlayers. H.H. also acknowledges support from the Wolfson Foundation, and the Royal Society.

Disclosures. H.H. is the founder, director, and a shareholder in PureLiFi, a company developing LiFi technology. The other authors declare no competing interests.

Research data supporting this publication is available at <http://doi.org/10.17630/2bde6593-32d5-47fe-849c-d34c3dabbe58>.

REFERENCES

1. NREL, "Best research-cell efficiencies," <https://www.nrel.gov/pv/assets/pdfs/best-research-cell-efficiencies.20190923.pdf>.
2. G. Grancini, C. Roldán-Carmona, I. Zimmermann, E. Mosconi, X. Lee, D. Martineau, S. Narbey, F. Oswald, F. De Angelis, M. Graetzel, and M. K. Nazeeruddin, "One-year stable perovskite solar cells by 2D/3D interface engineering," *Nat. Commun.* **8**, 15684 (2017).
3. C. Y. Chen, J. H. Chang, K. M. Chiang, H. L. Lin, S. Y. Hsiao, and H. W. Lin, "Perovskite photovoltaics for dim-light applications," *Adv. Funct. Mater.* **25**, 7064–7070 (2015).
4. L. K. Jagadamma, O. Blaszczyk, M. T. Sajjad, A. Ruseckas, and I. D. W. Samuel, "Efficient indoor p-i-n hybrid perovskite solar cells using low temperature solution processed NiO as hole extraction layers," *Sol. Energy Mater. Sol. Cells* **201**, 110071 (2019).
5. M. F. Müller, M. Freunek, and L. M. Reindl, "Maximum efficiencies of indoor photovoltaic devices," *IEEE J. Photovoltaics* **3**, 59–64 (2013).

6. L. Dou, Y. M. Yang, J. You, Z. Hong, W. H. Chang, G. Li, and Y. Yang, "Solution-processed hybrid perovskite photodetectors with high detectivity," *Nat. Commun.* **5**, 5404 (2014).
7. Q. Lin, A. Armin, D. M. Lyons, P. L. Burn, and P. Meredith, "Low noise, IR-blind organohalide perovskite photodiodes for visible light detection and imaging," *Adv. Mater.* **27**, 2060–2064 (2015).
8. S. Zhang, D. Tsonev, S. Videv, S. Ghosh, G. A. Turnbull, I. D. W. Samuel, and H. Haas, "Organic solar cells as high-speed data detectors for visible light communication," *Optica* **2**, 607–610 (2015).
9. S. Das, E. Poves, J. Fakidis, A. Sparks, S. Videv, and H. Haas, "Towards energy neutral wireless communications: photovoltaic cells to connect remote areas," *Energies* **12**, 3772 (2019).
10. J. Fakidis, S. Videv, H. Helmers, and H. Haas, "0.5-Gb/s OFDM-based laser data and power transfer using a GaAs photovoltaic cell," *IEEE Photon. Technol. Lett.* **30**, 841–844 (2018).
11. Z. Wang, D. Tsonev, S. Videv, and H. Haas, "Towards self-powered solar panel receiver for optical wireless communication," in *IEEE International Conference on Communications (ICC)* (2014), pp. 3348–3353.
12. C. Bao, J. Yang, S. Bai, W. Xu, Z. Yan, Q. Xu, J. Liu, W. Zhang, and F. Gao, "High performance and stable all-inorganic metal halide perovskite-based photodetectors for optical communication applications," *Adv. Mater.* **30**, 1803422 (2018).
13. M. Zhang, F. Zhang, Y. Wang, L. Zhu, Y. Hu, Z. Lou, Y. Hou, and F. Teng, "High-performance photodiode-type photodetectors based on polycrystalline formamidinium lead iodide perovskite thin films," *Sci. Rep.* **8**, 1 (2018).
14. G. Cen, Y. Liu, C. Zhao, G. Wang, Y. Fu, G. Yan, Y. Yuan, C. Su, Z. Zhao, and W. Mai, "Atomic-layer deposition-assisted double-side interfacial engineering for high-performance flexible and stable CsPbBr₃ perovskite photodetectors toward visible light communication applications," *Small* **15**, 1902135 (2019).
15. C. Li, J. Lu, Y. Zhao, L. Sun, G. Wang, Y. Ma, S. Zhang, J. Zhou, L. Shen, and W. Huang, "Highly sensitive, fast response perovskite photodetectors demonstrated in weak light detection circuit and visible light communication system," *Small* **15**, 1903599 (2019).
16. E. López-Fraguas, B. Arredondo, C. Vega-Colado, G. del Pozo, M. Najafi, D. Martín-Martín, Y. Galagan, J. M. Sánchez-Pena, R. Vergaz, and B. Romero, "Visible light communication system using an organic emitter and a perovskite photodetector," *Org. Electron.* **73**, 292–298 (2019).
17. L. Salamandra, N. Y. Nia, M. Di Natali, C. Fazolo, S. Maiello, L. La Notte, G. Susanna, A. Pizzoleo, F. Matteocci, L. Cinà, L. Mattiello, F. Brunetti, A. Di Carlo, and A. Reale, "Perovskite photodetectors (PVSK-PDs) for visible light communication," *Org. Electron.* **69**, 220–226 (2019).
18. C. H. Kang, I. Dursun, G. Liu, L. Sinatra, X. Sun, M. Kong, J. Pan, P. Maity, E. N. Ooi, T. K. Ng, O. F. Mohammed, O. M. Bakr, and B. S. Ooi, "High-speed colour-converting photodetector with all-inorganic CsPbBr₃ perovskite nanocrystals for ultraviolet light communication," *Light Sci. Appl.* **8**, 94 (2019).
19. Z. Wang, D. Tsonev, S. Videv, and H. Haas, "On the design of a solar-panel receiver for optical wireless communications with simultaneous energy harvesting," *IEEE J. Sel. Areas Commun.* **33**, 1612–1623 (2015).
20. M. Saliba, T. Matsui, J.-Y. Seo, K. Domanski, J.-P. Correa-Baena, M. K. Nazeeruddin, S. M. Zakeeruddin, W. Tress, A. Abate, A. Hagfeldt, and M. Grätzel, "Cesium-containing triple cation perovskite solar cells: improved stability, reproducibility and high efficiency," *Energy Environ. Sci.* **9**, 1989–1997 (2016).
21. A. Armin, M. Velusamy, P. Wolfer, Y. Zhang, P. L. Burn, P. Meredith, and A. Pivrikas, "Quantum efficiency of organic solar cells: electro-optical cavity considerations," *ACS Photon.* **1**, 173–181 (2014).
22. H. Baig, H. Kanda, A. M. Asiri, M. K. Nazeeruddin, and T. Mallick, "Increasing efficiency of perovskite solar cells using low concentrating photovoltaic systems," *Sustain. Energy Fuels* **4**, 528–537 (2020).
23. T. S. Sherkar, C. Momblona, L. Gil-Escrig, J. Ávila, M. Sessolo, H. J. Bolink, and L. J. A. Koster, "Recombination in perovskite solar cells: significance of grain boundaries, interface traps, and defect ions," *ACS Energy Lett.* **2**, 1214–1222 (2017).
24. D. Głowienka, D. Zhang, F. Di Giacomo, M. Najafi, S. Veenstra, J. Szymtkowski, and Y. Galagan, "Role of surface recombination in perovskite solar cells at the interface of HTL/CH₃NH₃PbI₃," *Nano Energy* **67**, 104186 (2020).
25. J. W. Matiko, N. J. Grabham, S. P. Beeby, and M. J. Tudor, "Review of the application of energy harvesting in buildings," *Meas. Sci. Technol.* **25**, 012002 (2014).
26. X. Tang, X. Wang, R. Cattley, F. Gu, and A. Ball, "Energy harvesting technologies for achieving self-powered wireless sensor networks in machine condition monitoring: a review," *Sensors* **18**, 4113 (2018).
27. R. Bian, I. Tavakkolnia, and H. Haas, "15.73 Gb/s visible light communication with off-the-shelf LEDs," *J. Lightwave Technol.* **37**, 2418–2424 (2019).
28. M. S. Islam, R. X. Ferreira, X. He, E. Xie, S. Videv, S. Viola, S. Watson, N. Bamiedakis, R. V. Penty, I. H. White, A. E. Kelly, E. Gu, H. Haas, and M. D. Dawson, "Towards 10 Gb/s orthogonal frequency division multiplexing-based visible light communication using a GaN violet micro-LED," *Photon. Res.* **5**, A35–A43 (2017).
29. L. M. Zhang and F. R. Kschischang, "Staircase codes with 6% to 33% overhead," *J. Lightwave Technol.* **32**, 1999–2002 (2014).
30. G. Richardson, S. E. J. O'Kane, R. G. Niemann, T. A. Peltola, J. M. Foster, P. J. Cameron, and A. B. Walker, "Can slow-moving ions explain hysteresis in the current-voltage curves of perovskite solar cells?" *Energy Environ. Sci.* **9**, 1476–1485 (2016).
31. D. A. Jacobs, H. Shen, F. Pfeffer, J. Peng, T. P. White, F. J. Beck, and K. R. Catchpole, "The two faces of capacitance: new interpretations for electrical impedance measurements of perovskite solar cells and their relation to hysteresis," *J. Appl. Phys.* **124**, 225702 (2018).
32. H. Xi, S. Tang, X. Ma, J. Chang, D. Chen, Z. Lin, P. Zhong, H. Wang, and C. Zhang, "Performance enhancement of planar heterojunction perovskite solar cells through tuning the doping properties of hole-transporting materials," *ACS Omega* **2**, 326–336 (2017).
33. S. H. Turren-Cruz, M. Saliba, M. T. Mayer, H. Juárez-Santiesteban, X. Mathew, L. Nienhaus, W. Tress, M. P. Erodici, M. J. Sher, M. G. Bawendi, M. Grätzel, A. Abate, A. Hagfeldt, and J. P. Correa-Baena, "Enhanced charge carrier mobility and lifetime suppress hysteresis and improve efficiency in planar perovskite solar cells," *Energy Environ. Sci.* **11**, 78–86 (2018).
34. H. H. Wang, Q. Chen, H. Zhou, L. Song, Z. St Louis, N. De Marco, Y. Fang, P. Sun, T. Bin Song, H. Chen, and Y. Yang, "Improving the TiO₂ electron transport layer in perovskite solar cells using acetylacetonate-based additives," *J. Mater. Chem. A* **3**, 9108–9115 (2015).